Electronic Supplementary Information

Tuning Electrical Properties of Graphene Oxide through Low-Temperature Thermal Annealing

Cataldo Valentini,[a] Verónica Montes-García,[a] Pietro Antonio Livio,[a] Tomasz Chudziak,[b,c] Jésus Raya,[d] Artur Ciesielski,[a,b] and Paolo Samorì*[a]*

Table of contents

Table S1. State-of-the-art of the thermal annealing conditions of GO at low temperatures.

Sample	Ambient	Temperature (°C)	Time	Resistivity / Sheet Resistance	Reference
Film	UHV	125-240	17 h	n.a.	[1]
Film	UHV	150	15 min	~10 Ωm	[2]
Film	UHV	200	15 min	~10^{-2} Ωm	[2]
Film	Ar/H_2	200	15 min	~10^{-2} Ωm	[2]
Film	Ar/H_2	600	15 min	~10^{-4} Ωm	[2]
Film	Ar/H_2	1100	15 min	~10^{-5} Ωm	[2]
Film	N_2H_4 vapour	80	7 h	~10^{-3} Ωm	[2]
Film	1) N_2H_4 vapour 2) Ar/H_2	1) 80 2) 200	1) 24 h 2) 15 min	~10^{-4} Ωm	[2]
Film	1) N_2H_4 vapour 2) Ar/H_2	1) 80 2) 1100	1) 24 h 2) 15 min	~10^{-5} Ωm	[2]
Film	UHV	200	2 h	10^{-2} Ωm	[3]
N,N-dimethylacetamide solution	N_2	150	5 h	n.a.	[4]
Powder or aqueous solution	Aqueous in a autoclave, vacuum, or air	95-150	15 h	n.a.	[5]
Powder	N_2	150	2 h	48 Ωm	[6]
Powder	N_2	200	2 h	$2\cdot10^{-3}$ Ωm	[6]
Powder	N_2	500	2 h	$5\cdot10^{-4}$ Ωm	[6]
Powder	N_2	900	2 h	10^{-3} Ωm	[6]
Powder	Vacuum	80	5 days	10^{5} Ωsq^{-1}	[7]
Film	N_2	75-250	45 min	n.a.	[8]
Film	Vacuum	200	12h	n.a.	[9]
Powder	Air	300	2h	n.a.	[10]
Film	Air	100-250	15 min	$4\cdot10^{-2}$ Ωm	[11]
Film	Air	70-300	15 min	n.a.	[12]
Film	Ar/H_2	100-500	10 min	n.a.	[13]
Film	Air or Ar	130-300 °C	4 and 24 h	10^{-2} – 10^{-4} Ωm	This work

UHV=Ultrahigh vacuum; n.a. = not available

1. TGA characterization

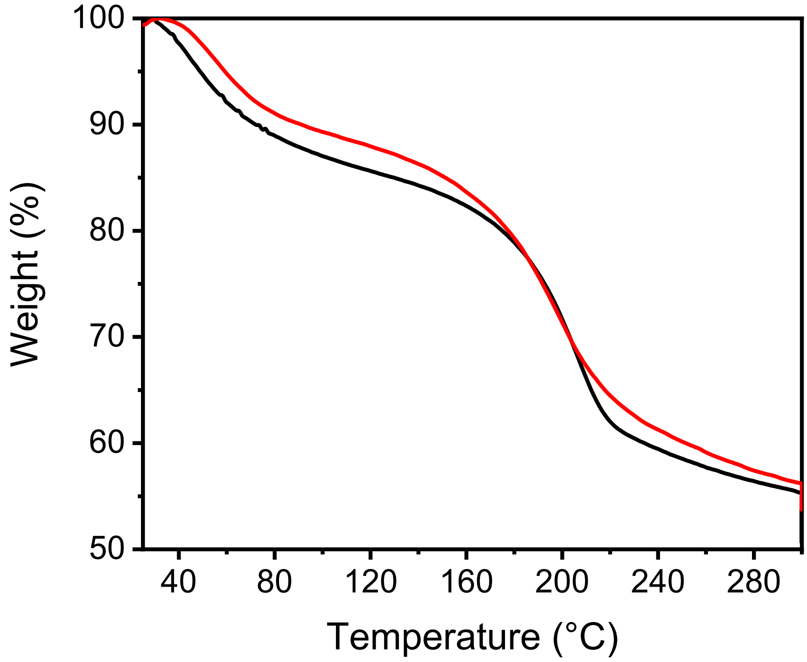

Figure S1. TGA diagram for the annealing of GO under air (black curve) and N_2 (red curve).

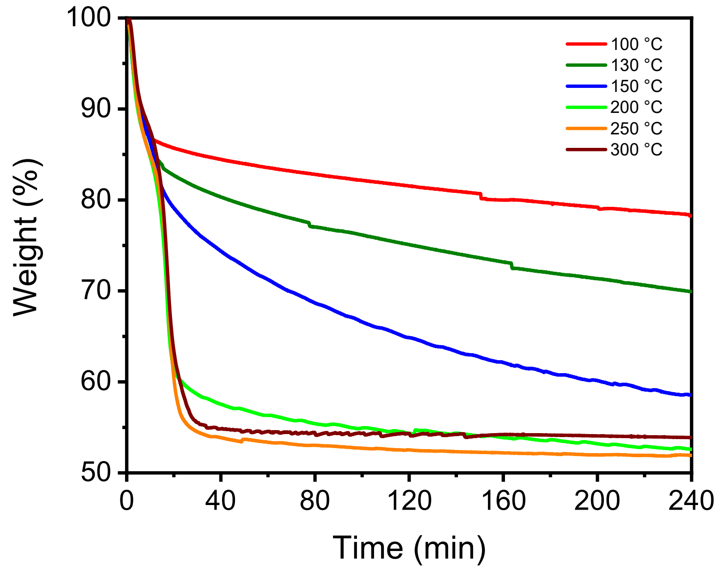

Figure S2. Kinetic TGA for the annealing of GO under N_2 at different temperatures during 4h.

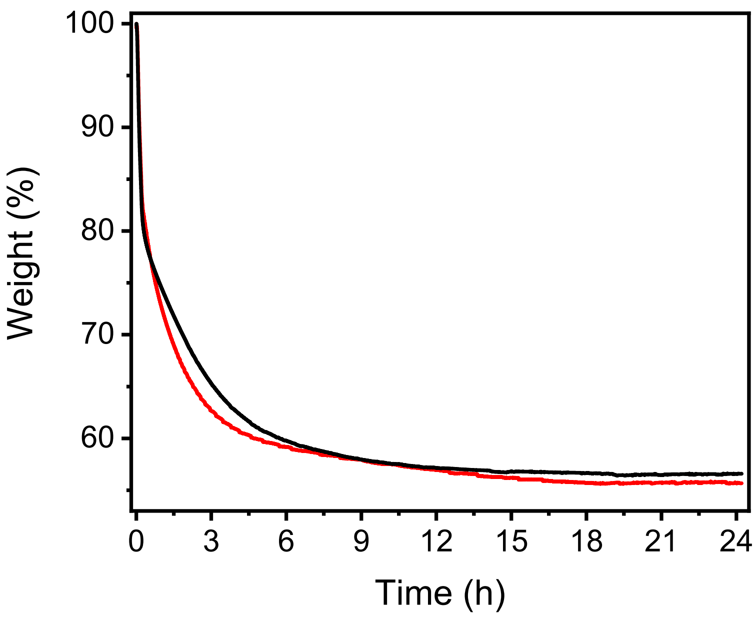

Figure S3. Kinetic TGA for the annealing of GO under air (black curve) and N_2 (red curve) at 150ºC for 24h.

2. AFM characterization

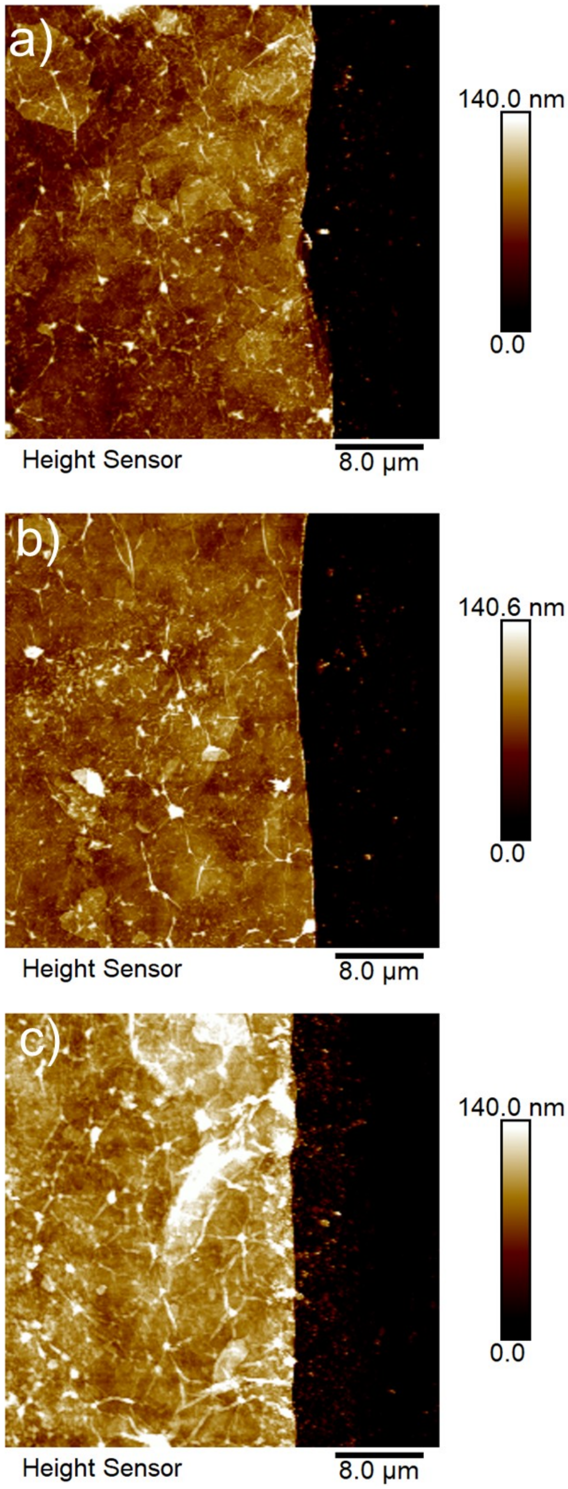

Figure S4. AFM images of pristine GO films a) sample 1, b) sample 2 and c) sample 3.

Table S2. Film thickness calculated from AFM images.

Conc (mg/mL)	Sample 1 (nm)	Sample 2 (nm)	Sample 3 (nm)	Avg (nm)	σ (nm)
10	78.5	65.87	55.4	66	11

3. Resistivity characterization

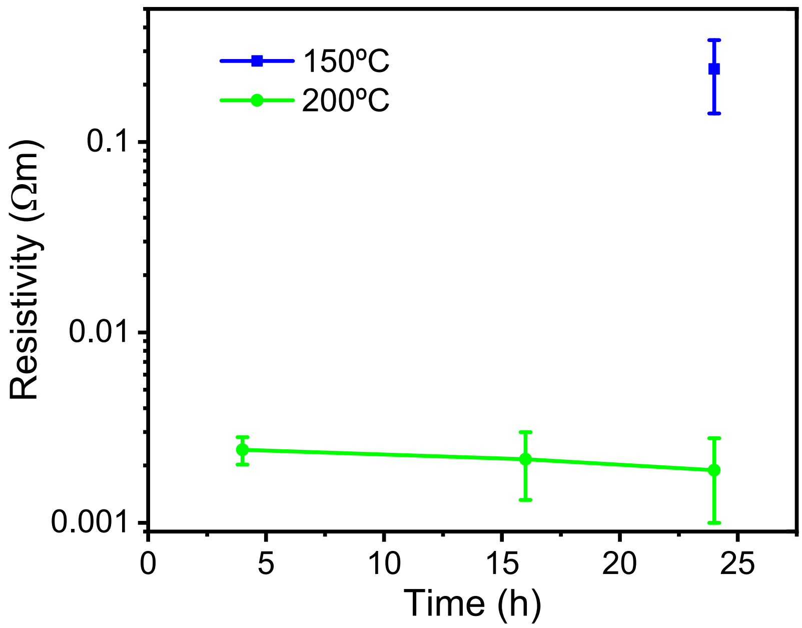

Figure S5. Kinetic resistivity measurements for the annealing of GO under argon at 150ºC and 200ºC.

4. Bending characterization

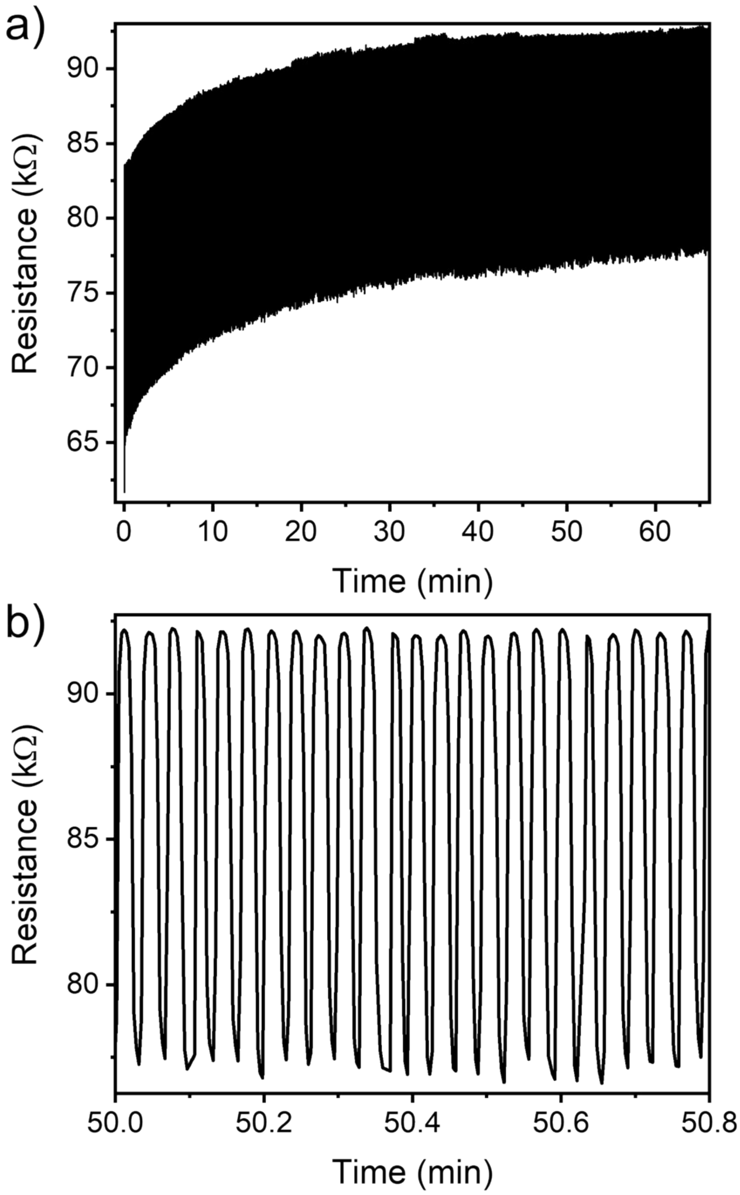

Figure S6. a) Resistance of the film as a function of time during the application of 2000 bending cycles with a bending radius of 6 mm, b) magnification of the film resistance as a function of time.

5. XPS characterization

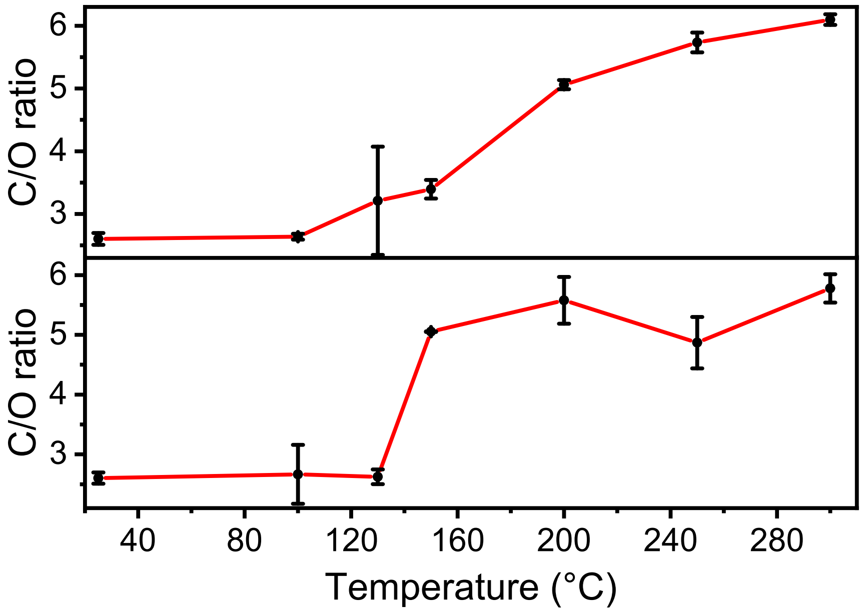

Figure S7. C/O ratio obtained from the XPS analysis of the TrGO under N_2 (top) and air (bottom).

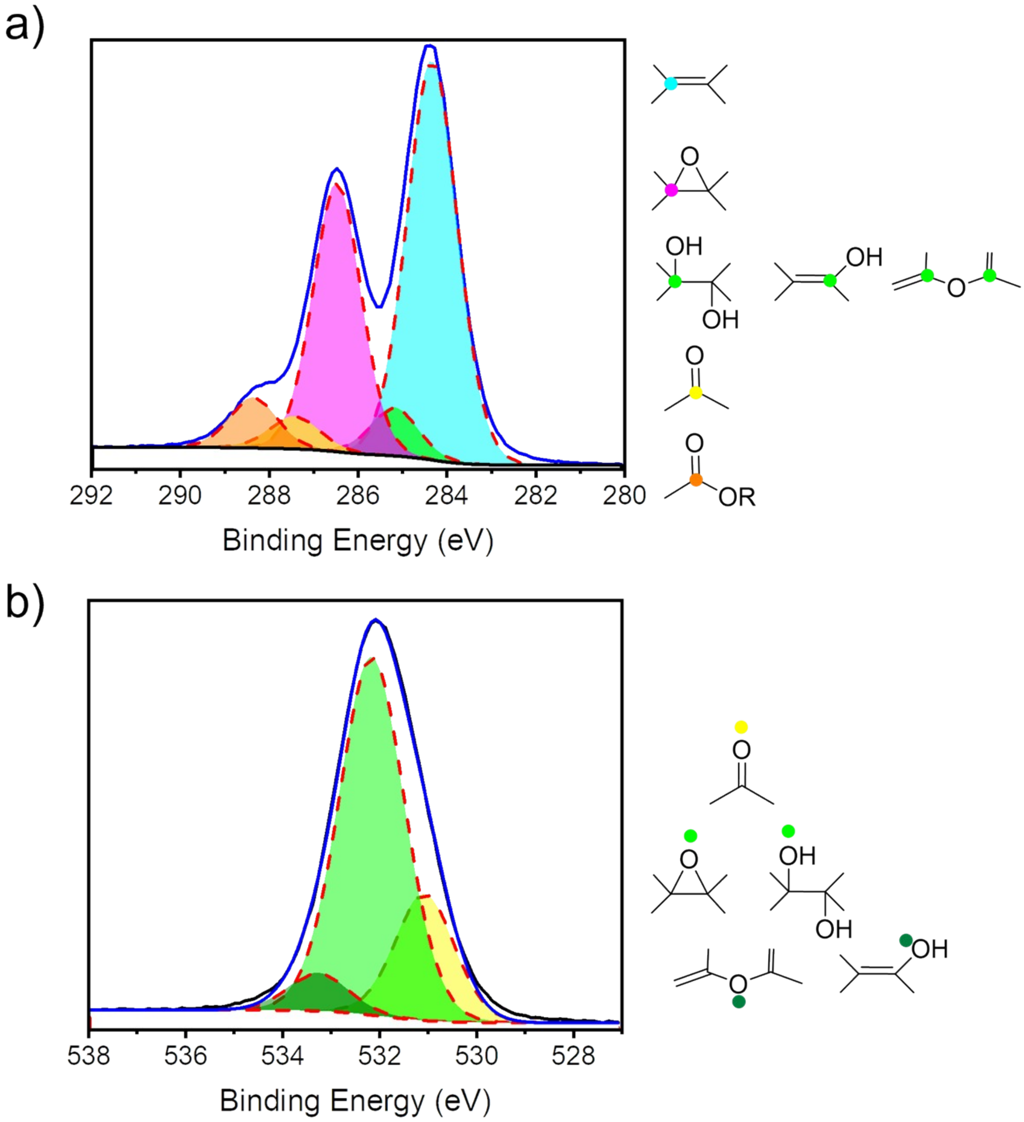

Figure S8. Fitted XPS a) C1s and b) O1s spectrum of GO and their corresponding chemical groups.

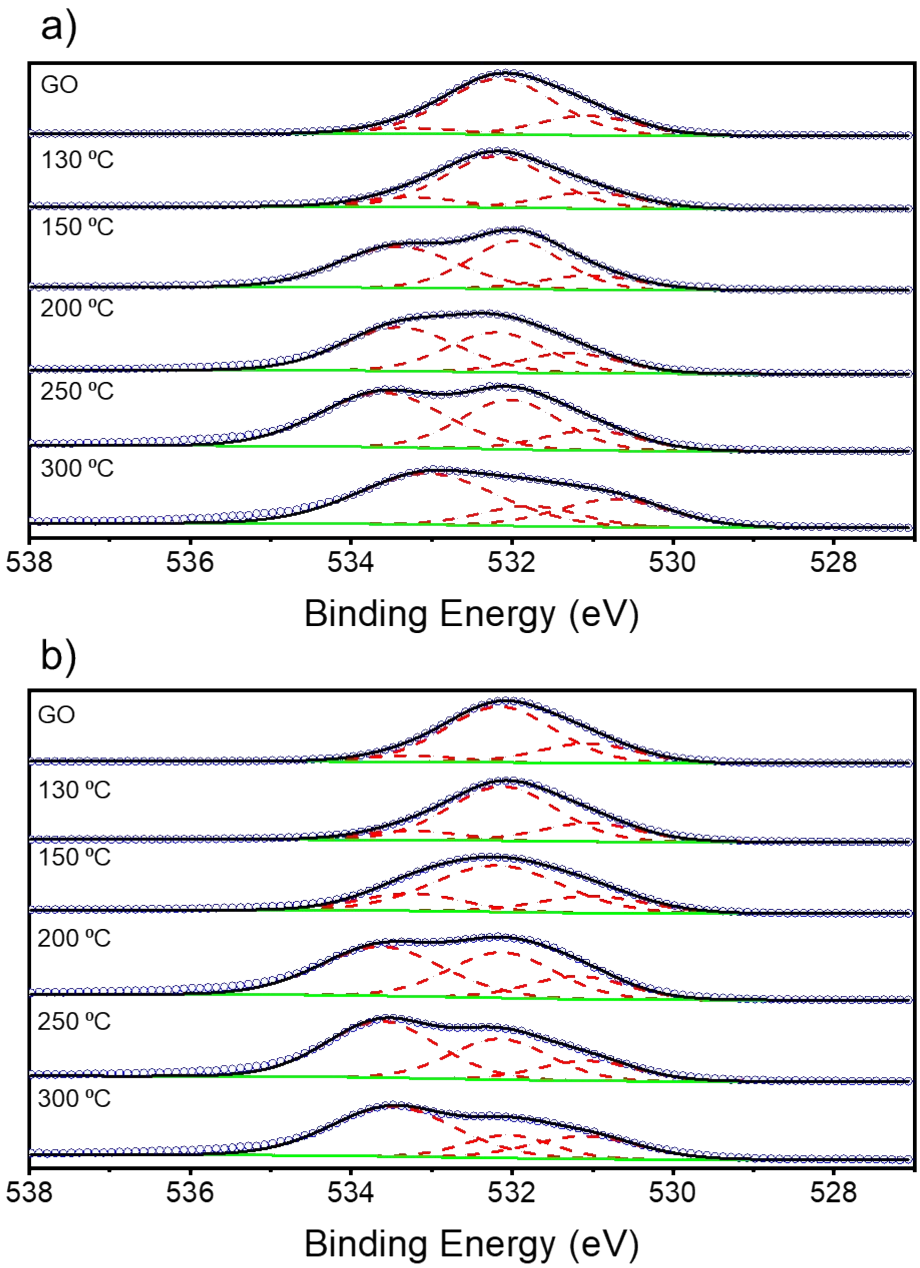

Figure S9. XPS analysis of O1s for the TrGO under (a) air and (b) N_2.

6. NMR characterization

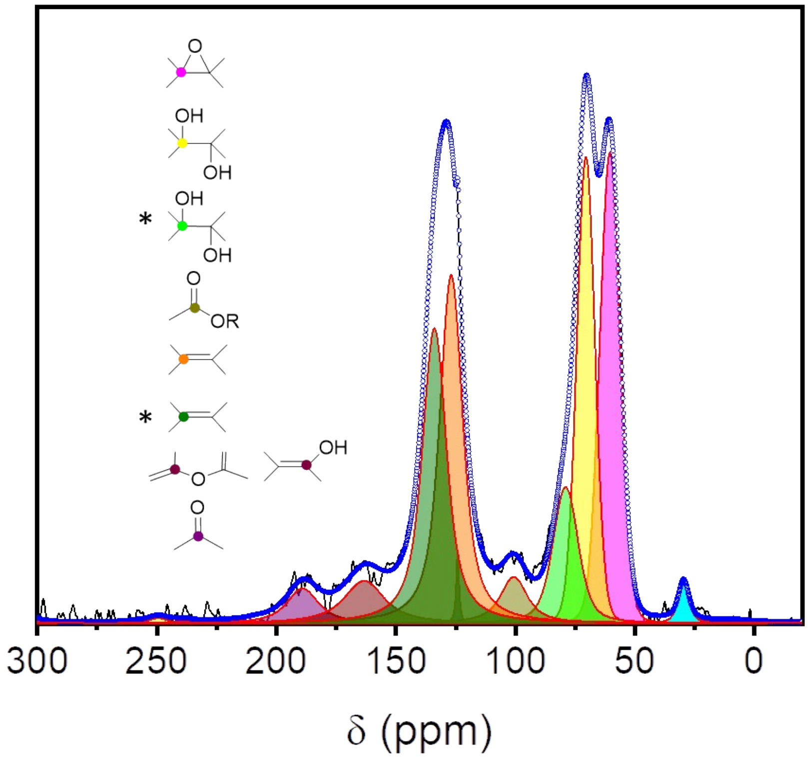

Figure S10 Fitted ssNMR spectrum of GO and their corresponding chemical groups. The stars refer to the chemical groups close to defects.

7. Raman characterization

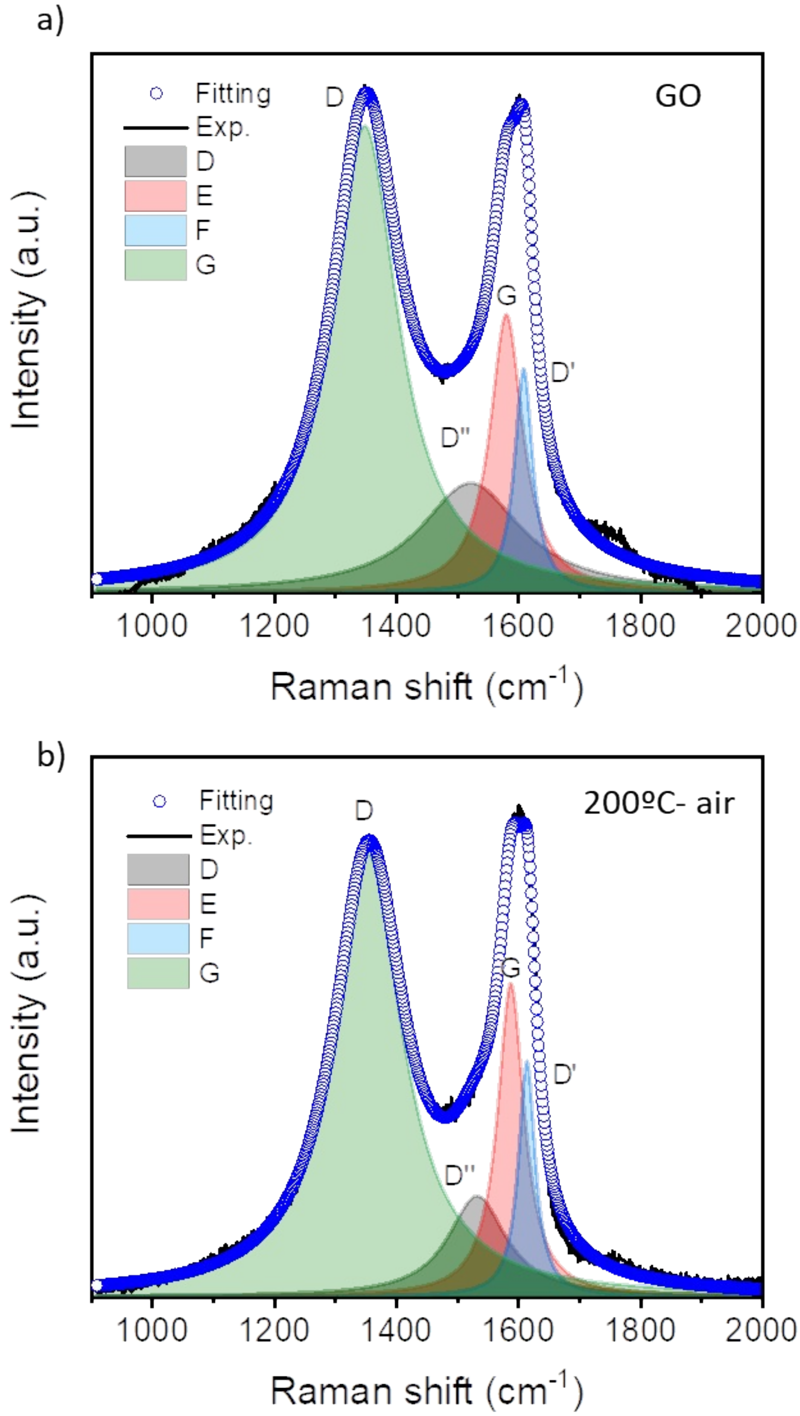

Figure S11. Fitted Raman spectra of (a) GO and (b) TrGO at 200ºC under air.

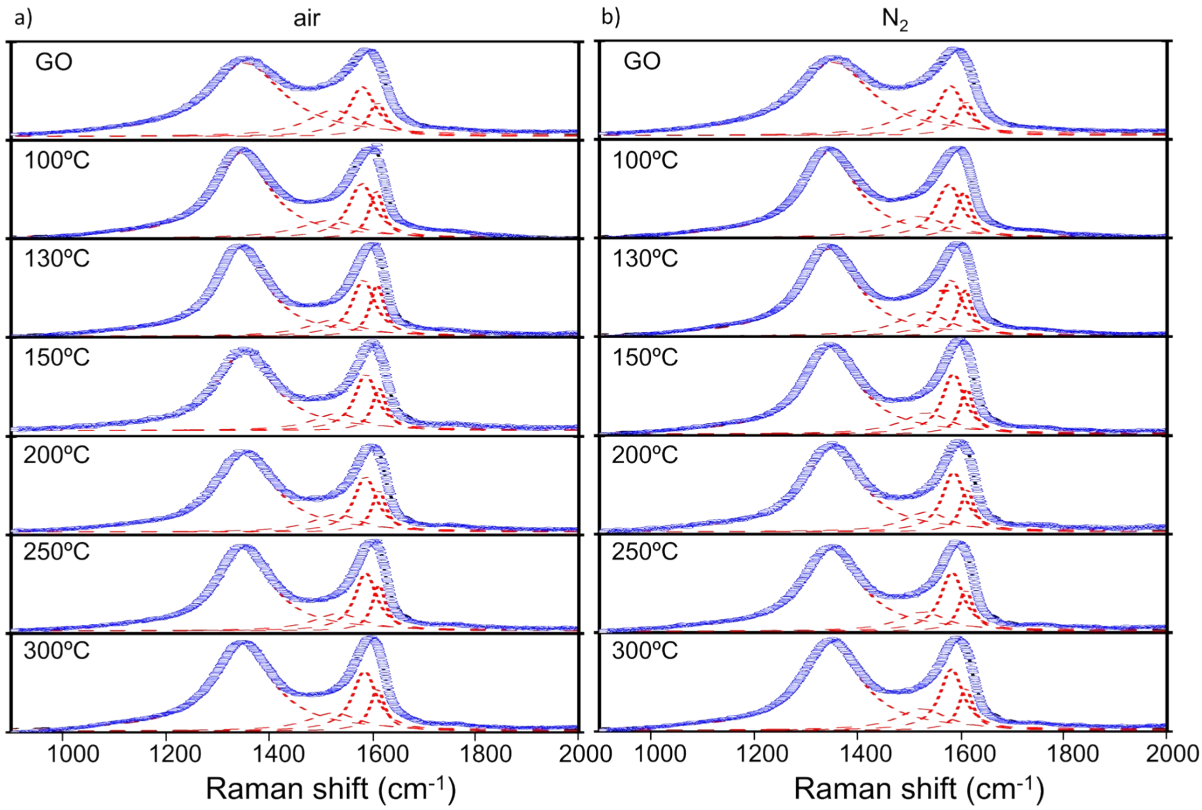

Figure S12. Fitted Raman spectra of GO and TrGO under (a) air and (b) under N_2 at different temperatures.

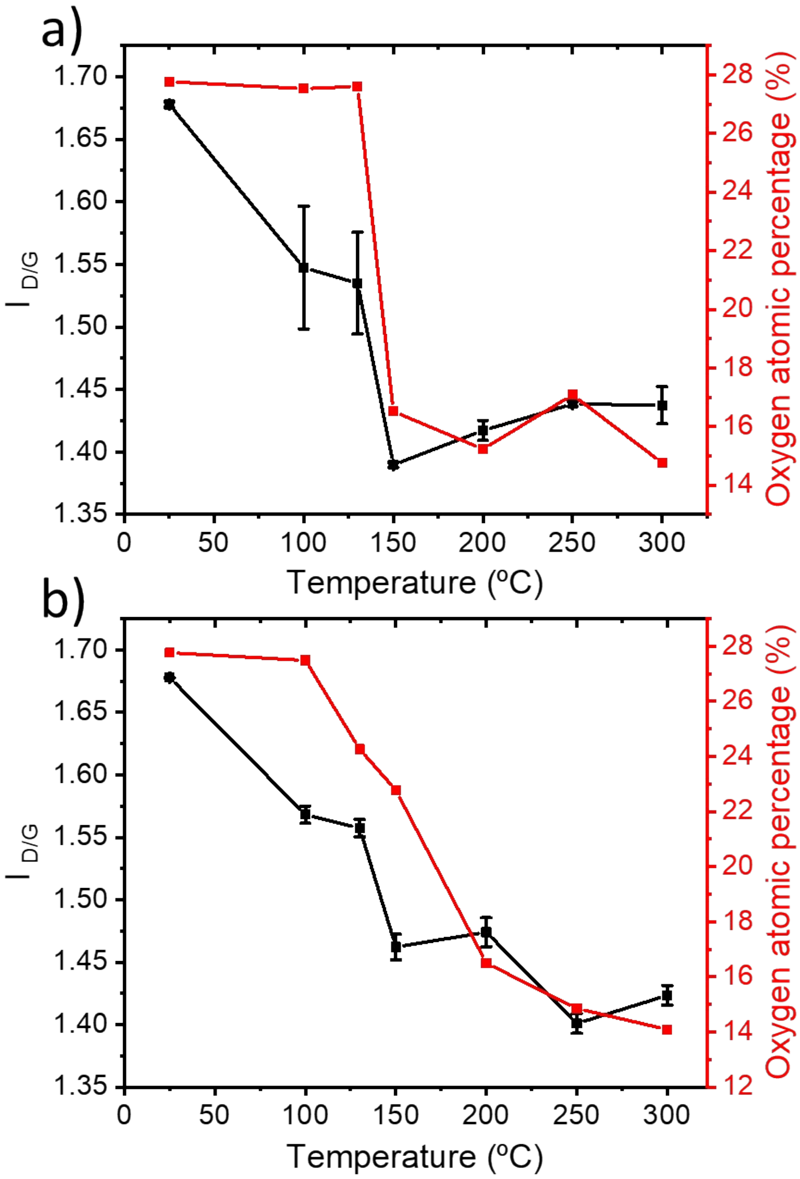

Figure S13. Evolution of the $I_{D/G}$ ratio values and the oxygen atomic percentage of TrGO as a function of the annealing temperature under (a) air and (b) under N_2.

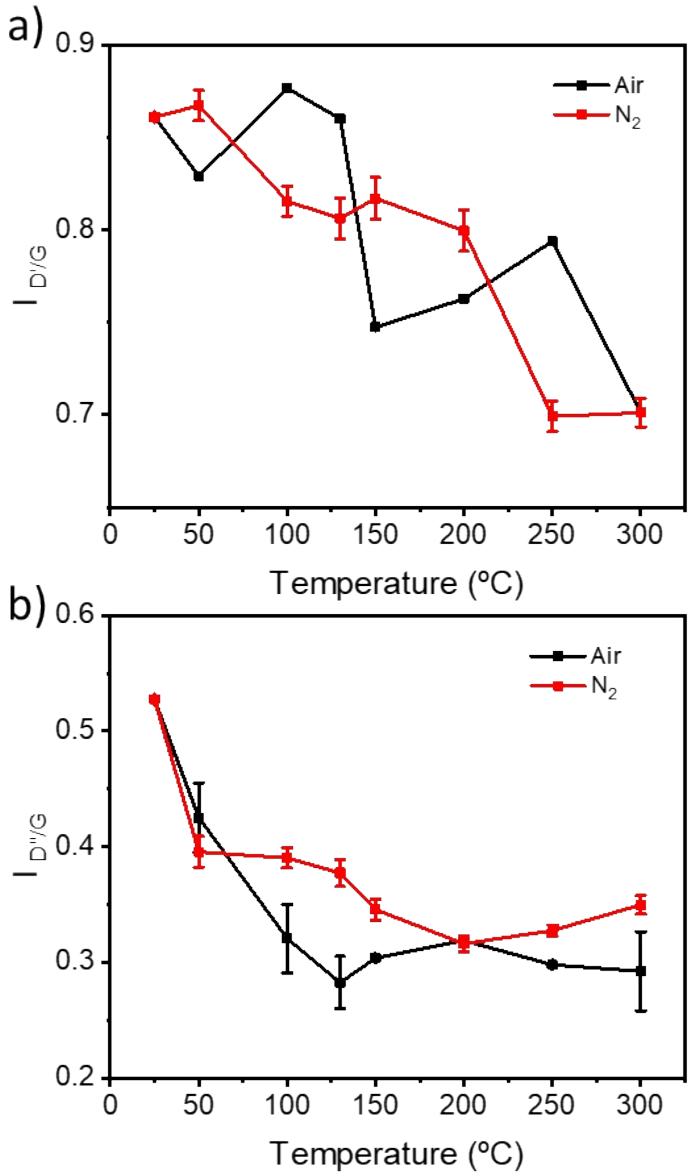

Figure S14. Evolution of the (a) $I_{D'/G}$ and (b) $I_{D''/G}$ ratio values of TrGO as a function of the annealing temperature under air (black curves) and under N_2 (red curves).

Table S3. Fitting parameters calculated for GO and TrGO Raman spectra under air.

Air	D''		G		D'		D	
T(ºC)	Rs(cm^{-1})	w(cm^{-1})	Rs (cm^{-1})	w(cm^{-1})	Rs (cm^{-1})	w(cm^{-1})	Rs (cm^{-1})	w(cm^{-1})
25	1523.1	200.0	1581.6	66.1	1610.2	36.5	1349.3	135.0
50	1523.7	198.4	1581.0	63.7	1610.2	36.1	1349.2	134.8
100	1518.8	143.1	1582.1	61.2	1610.4	33.6	1349.2	130.9
130	1526.9	120.1	1585.3	54.6	1611.9	33.6	1348.1	120.8
150	1534.2	113.0	1589.9	52.5	1616.0	32.9	1354.2	136.4
200	1533.6	115.5	1589.1	53.5	1615.5	33.4	1354.7	139.5
250	1536.1	115.6	1589.9	51.4	1615.4	31.8	1352.7	127.8
300	1527.8	121.0	1587.5	56.1	1612.6	34.2	1351.3	138.6

Rs: Raman shift; w: width.

Table S4. Fitting parameters calculated for GO and TrGO Raman spectra under N_2.

N_2	D''		G		D'		D	
T(ºC)	Rs(cm^{-1})	w(cm^{-1})	Rs (cm^{-1})	w(cm^{-1})	Rs (cm^{-1})	w(cm^{-1})	Rs (cm^{-1})	w(cm^{-1})
25	1523.1	200.0	1581.6	66.1	1610.2	36.5	1349.3	135.0
50	1527.6	124.6	1580.0	57.9	1608.3	37.3	1349.4	133.5
100	1522.3	133.2	1580.0	61.2	1609.1	36.9	1347.8	132.0
130	1530.8	118.5	1584.3	55.1	1611.3	33.8	1348.0	132.7
150	1536.4	114.6	1588.6	52.1	1614.3	31.6	1350.6	130.7
200	1536.9	108.6	1589.1	52.6	1615.6	31.6	1352.8	137.9
250	1529.8	110.4	1586.1	53.6	1612.8	33.5	1351.5	136.6
300	1528.6	114.0	1585.2	54.6	1613.0	33.4	1351.7	138.7

8. PXRD characterization

PXRD diffractograms have been acquired using a D8 Advanced with twin-twin optics (Bruker). The diffraction patterns of the powder samples have been acquired in 5-40 (2θ) range in Bragg-Brentano configuration, using $Cu_{K\alpha}$ radiation and a LINXEYE 2 detector. Two 2.5 mm Soller Cu slits have been applied to the primary and secondary optics. In the latter, a Ni stopper has been added to filter $Cu_{k\beta}$ radiations. An automatized blade has been mounted to limit the contribution of air scattering at low angles. The data has been acquired with a step of 0.02° and an acquisition time of 0.2 s per step.

Calculation of the XRD parameters

From the XRD diffractograms the peak position has been calculated using the Bragg's law:

$$d_{(hkl)} = \frac{\lambda}{2\sin\theta} \tag{1}$$

Where $d_{(hkl)}$ is the calculated inter planar distance (Å), λ is the wavelength of the XRD source (Å), θ is the scattering angle (rad). The crystallite dimension has been derived from the Scherrer formula:

$$L_C = \frac{K\lambda}{\beta\cos\theta} \tag{2}$$

Where Lc is the crystallite dimension (Å), K is the shape factor equal to 0.89,[14] β is the FWHM of the diffraction peak (rad)

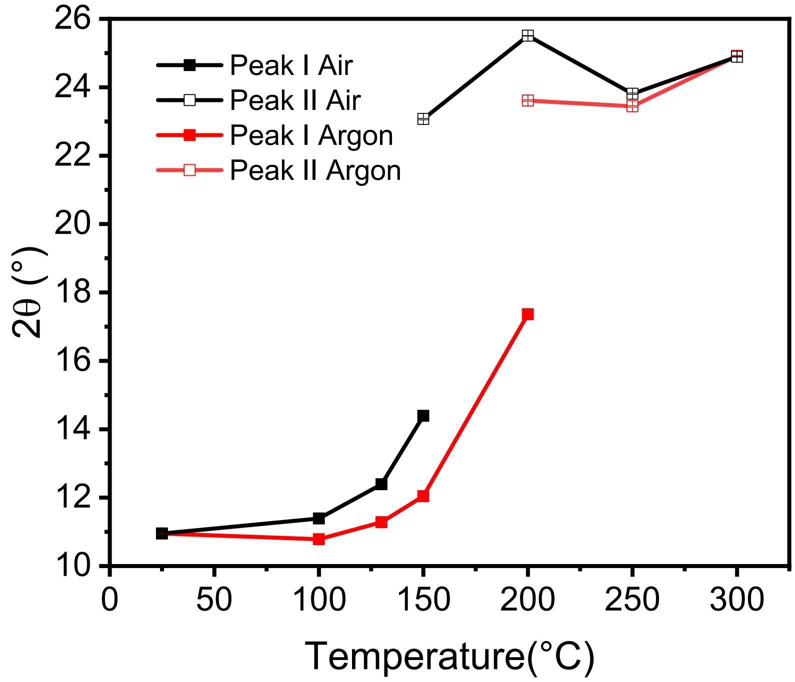

Figure S15. Main peak position for GO and TrGO under air (black curves) and under argon (red curves).

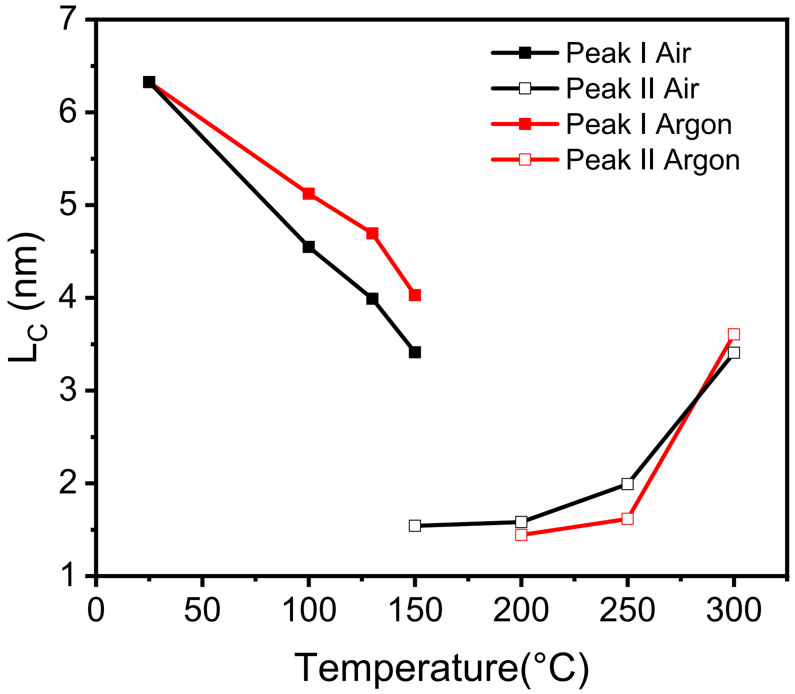

Figure S16. Crystallite size calculated for GO and TrGO under air (black curves) and under argon (red curves).

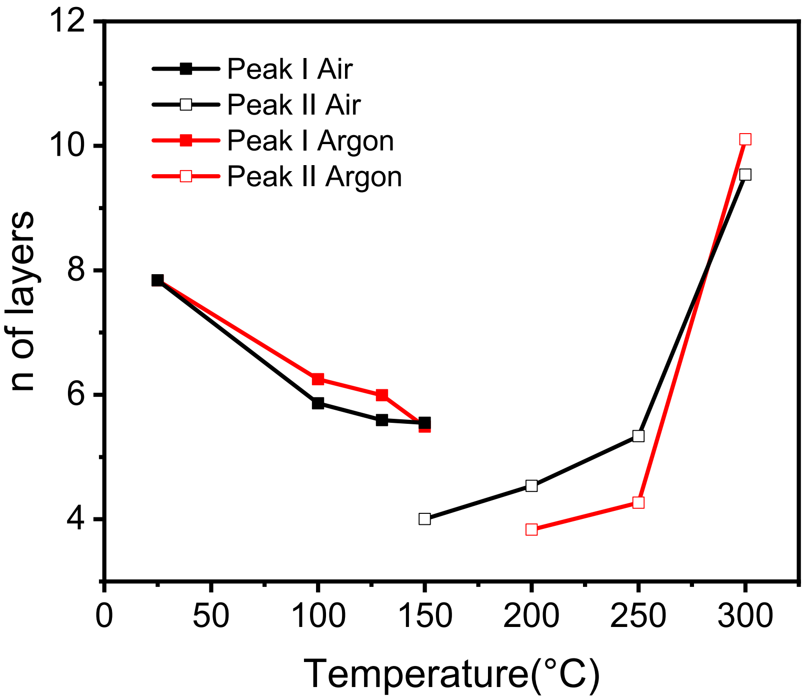

Figure S17. Number of GO layers for GO and TrGO under air (black curves) and under argon (red curves).

9. BET characterization

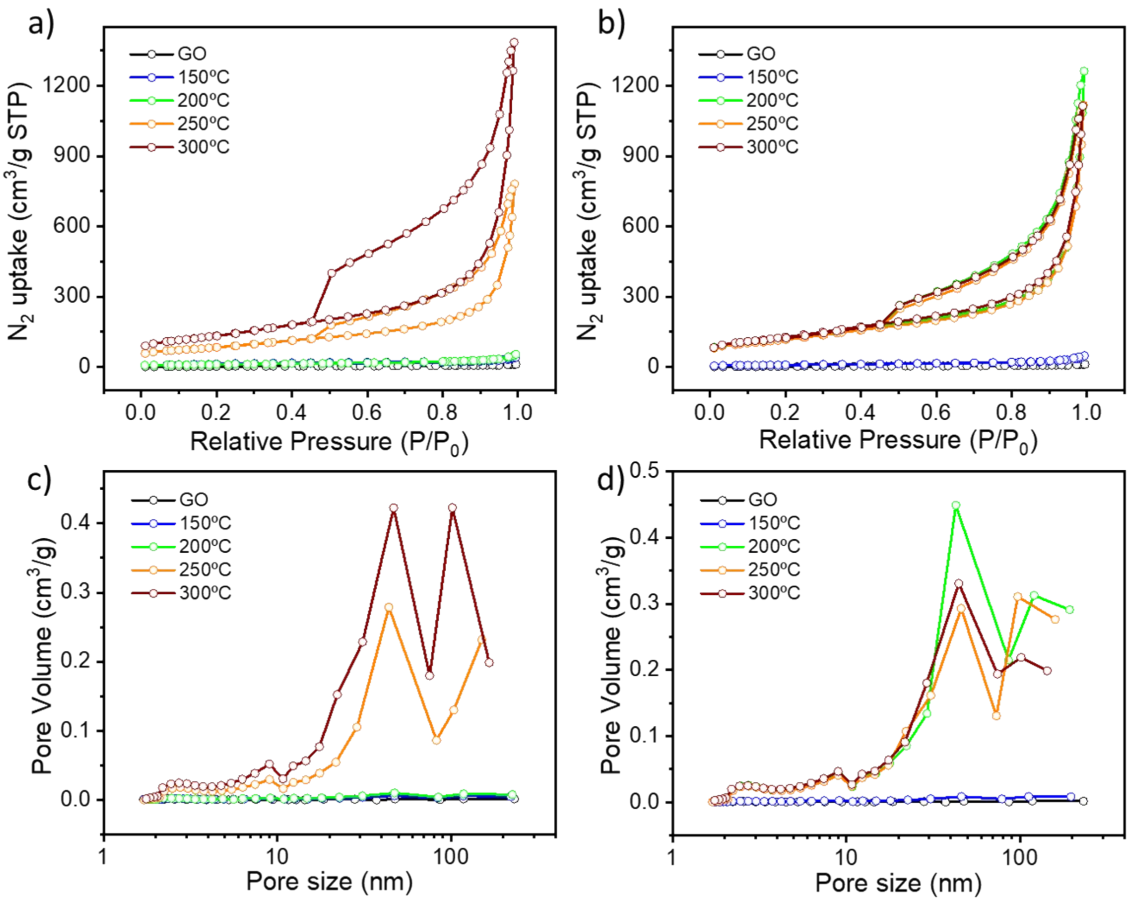

Figure S18. BET surface area of GO and TrGO under (a) air and (b) argon. Pore size distribution of thermally-reduced GO under (c) air and (d) argon.

Table S5. Average surface area and pore size of GO and TrGO.

	Air annealing		Argon annealing	
Temperature	Surface area (m^2/g)	Pore size (nm)	Surface area (m^2/g)	Pore size (nm)
GO	12.61	6.95	12.61	6.95
150	32.40	8.78	35.14	8.71
200	44.28	7.92	439.92	16.63
250	302.59	15.13	420.72	15.51
300	480.44	16.53	462.57	13.90

10. Photoelectron Yield Spectroscopy in Air (PYSA) characterization

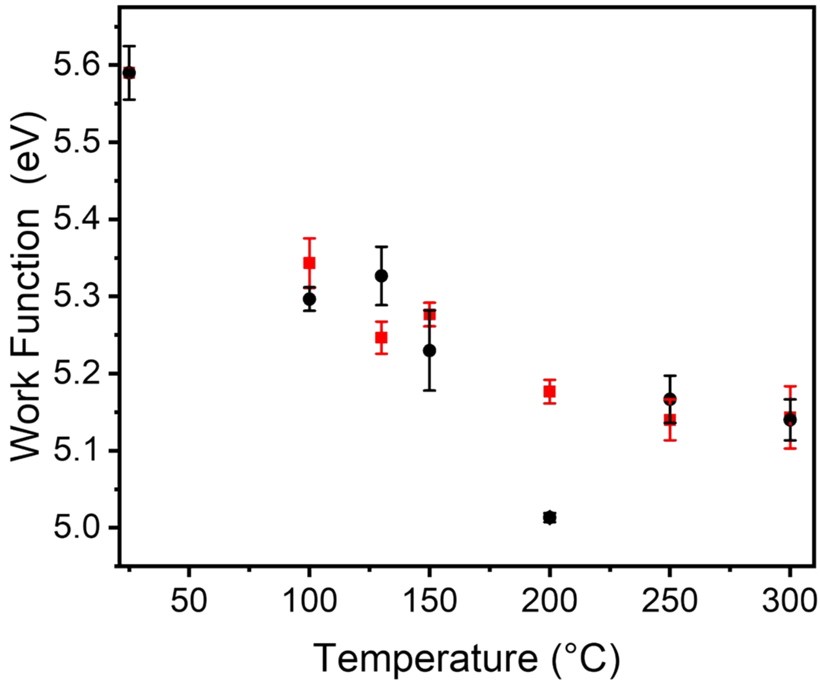

Figure S19. Work function of (Tr)GO annealed under air (black dots) and argon (red dots) at different temperatures for 4 hours.

11. Electrochemical characterization

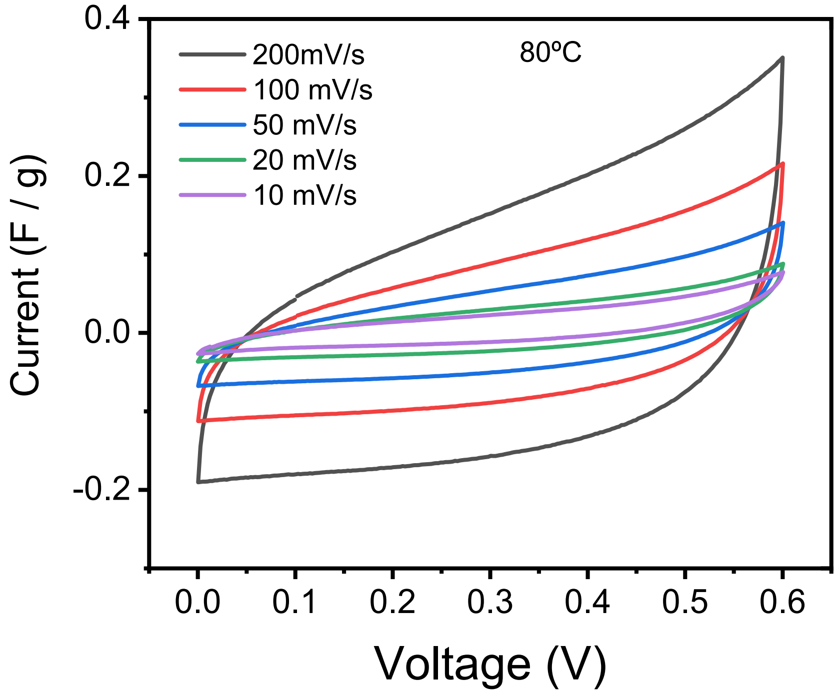

Figure S20. CV curves of GO at different scan rates.

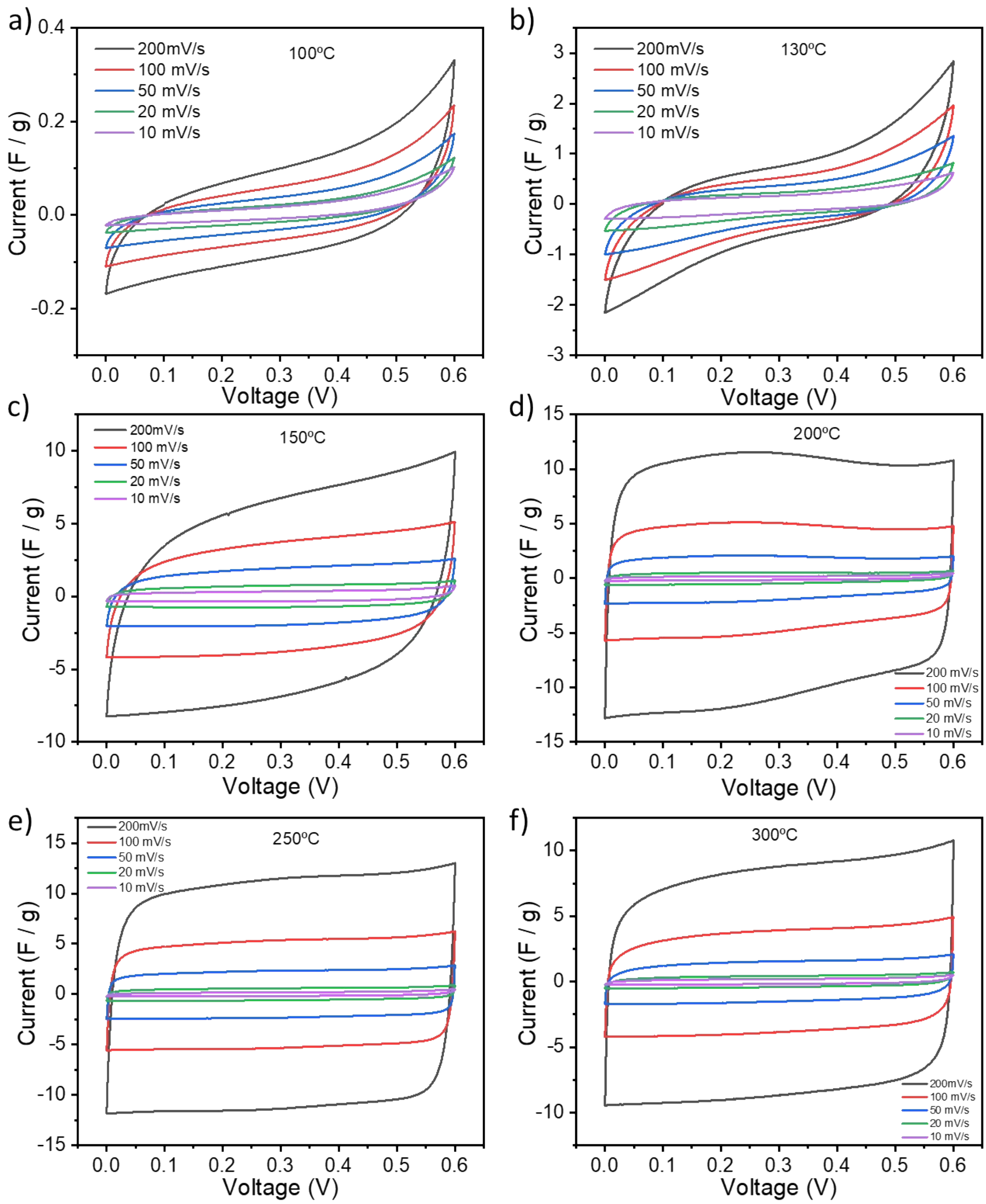

Figure S21. CV curves of TrGO under air at different scan rates.

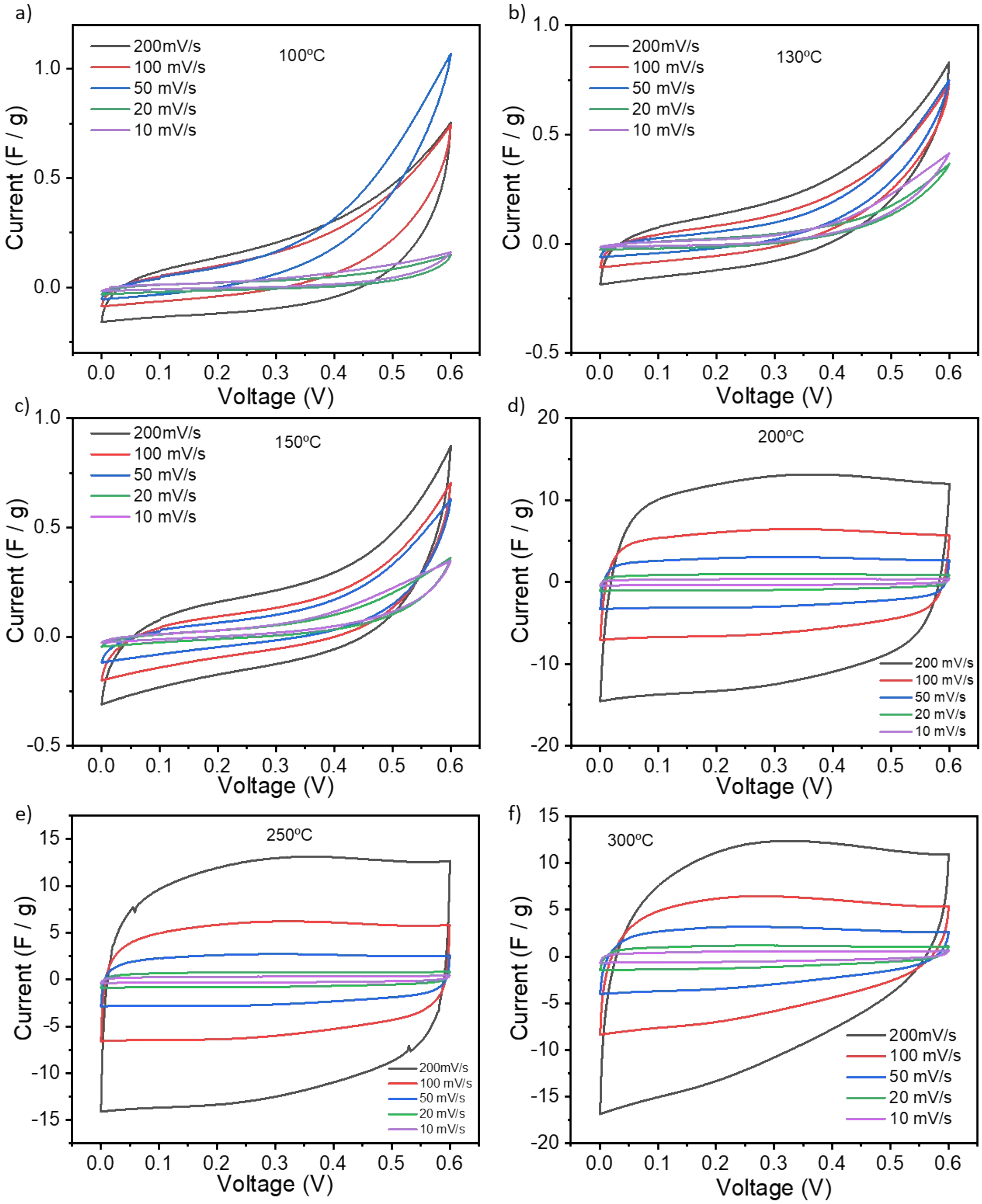

Figure S22. CV curves of TrGO under argon at different scan rates.

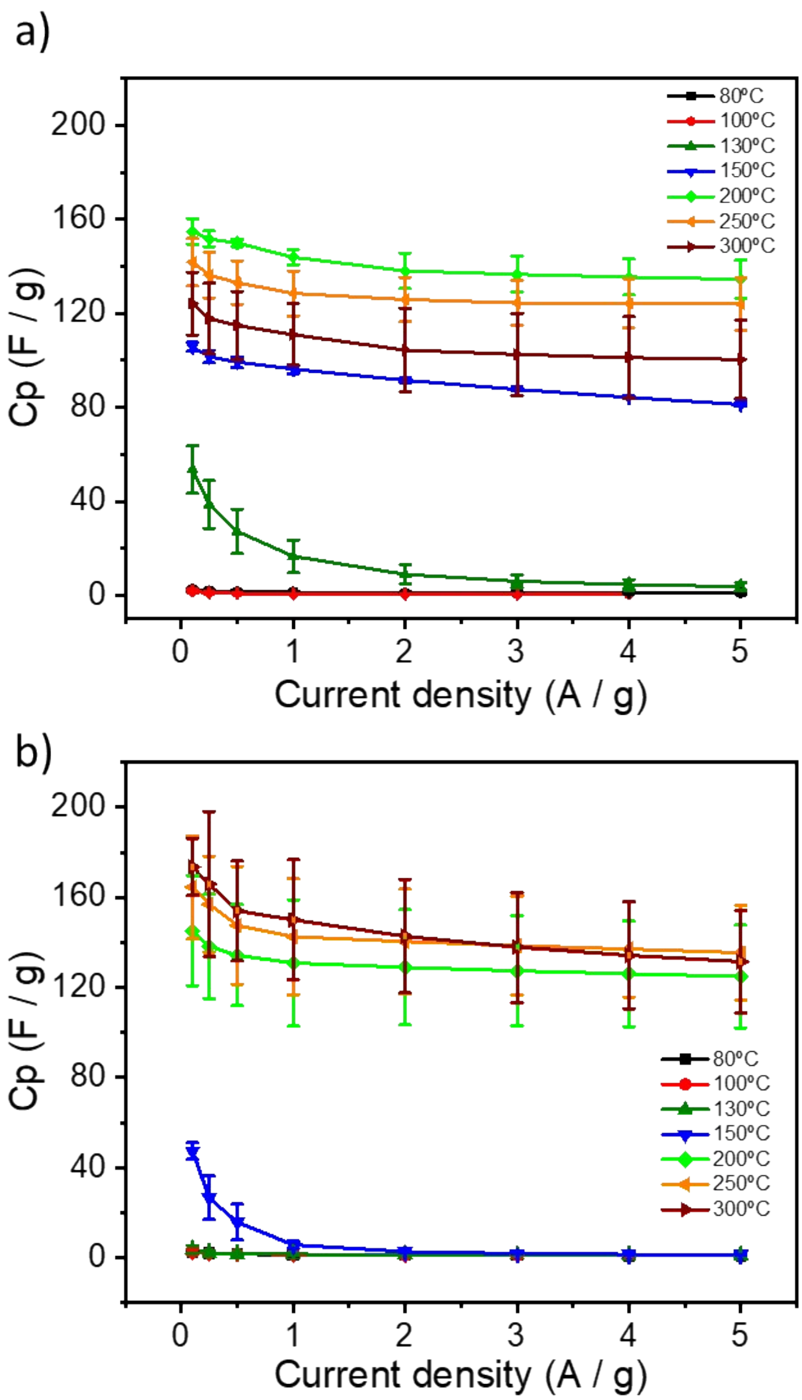

Figure S23. Comparison of specific capacitances versus current densities of TrGO under (a) air and (b) under argon.

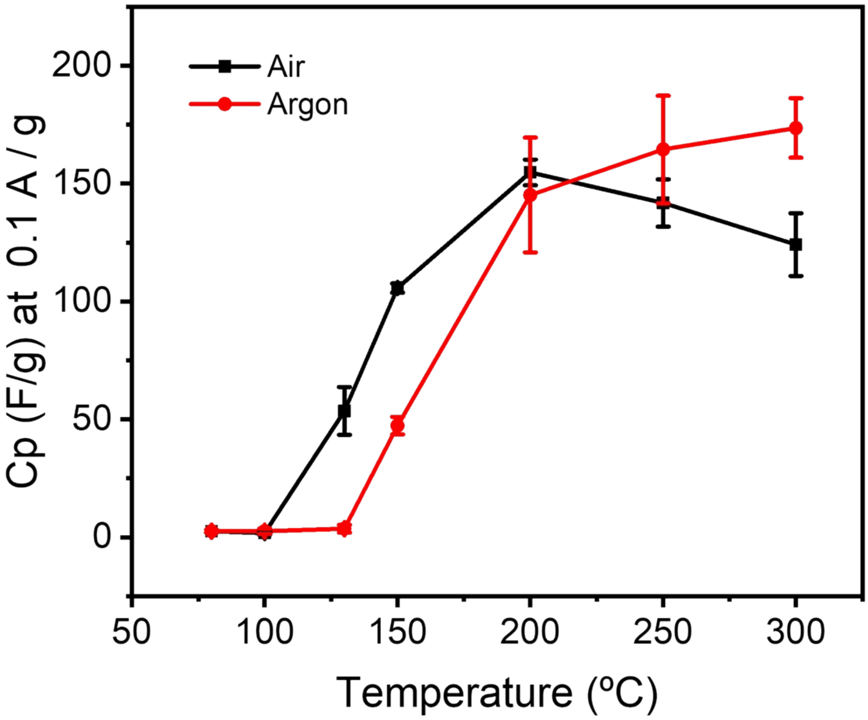

Figure S24. Specific capacitances at 0.1 A/g of TrGO under air (black curve) and under argon (red curve).

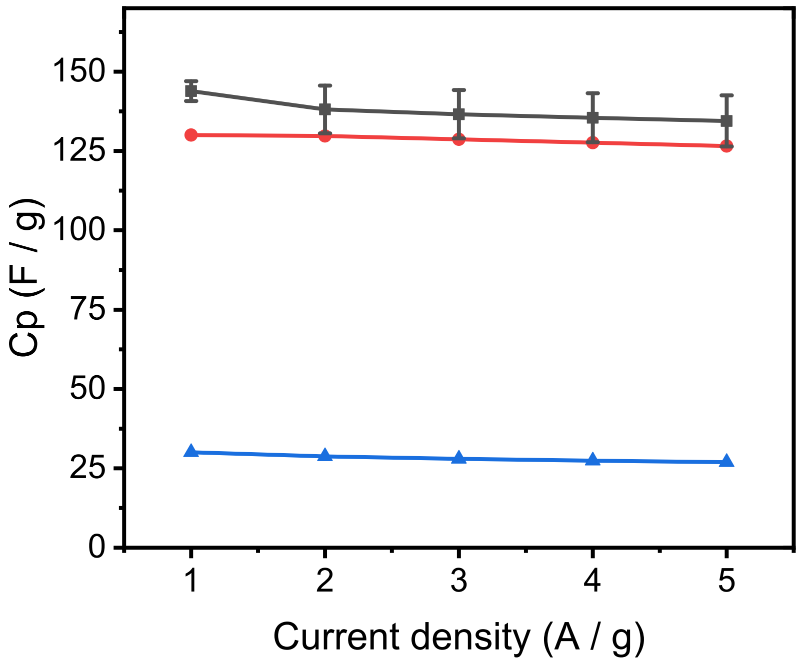

Figure S25. Comparison of specific capacitances versus current densities by using KOH 6 M (black curve), H_2SO_4 1 M (red curve) and tetraethylammonium tetrafluoroborate 1M in acetonitrile (blue curve) as electrolytes.

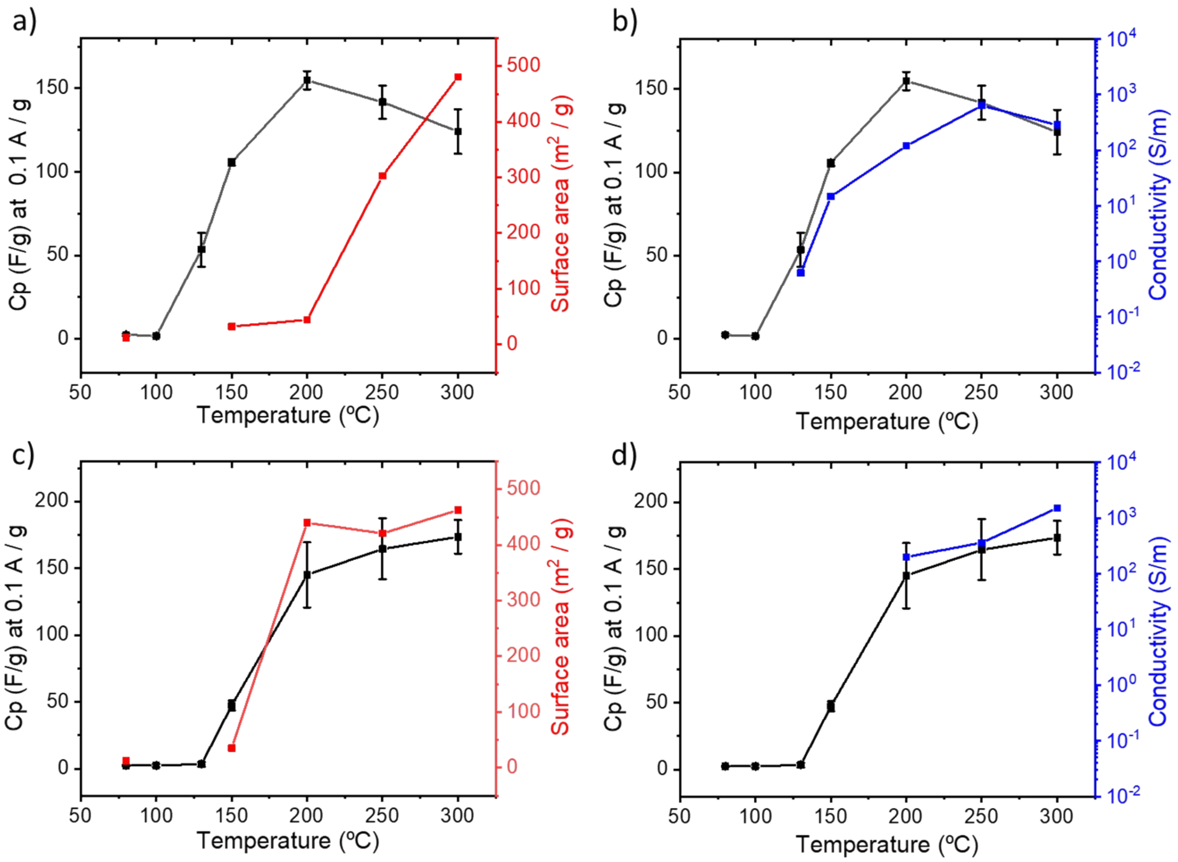

Figure S26. Specific capacitances at 0.1 A/g of TrGO (a, b) under air and (c, d) under argon compared with their corresponding (a, c) surface area and (b, d) film conductivity. Film conductivities were calculated by the inverse of the film resistivity of Figure 1c.

Table S6. State of the art TrGO as supercapacitors.

Annealing temperature (ºC)	Time	Atmosphere	Capacitance (F/g)	Electrolyte	Surface area (m^2/g)	Reference
200	4 hours	Air	208 ± 3.2	6 M KOH	325.1 ± 24.1	This work
300	4 hours	Argon	177.1 ± 29.6	6 M KOH	347.3 ± 17.6	
200	5 hours	High vacuum	264	30% KOH	400	[15]
200	2 hours	N_2	260	6 M KOH	71.50	[6]
400	1 hour	Air	206	1 M KOH	-	[16]
200	50 min	Air	165	0.5 M H_2SO_4	-	[17]
200	12 hours	N_2	132	1 M H_2SO_4		[18]
400	110 min	N_2	96	5 M H_2SO_4	429	[19]
200	1 hour	Argon	201	5 M KOH	248	[20]

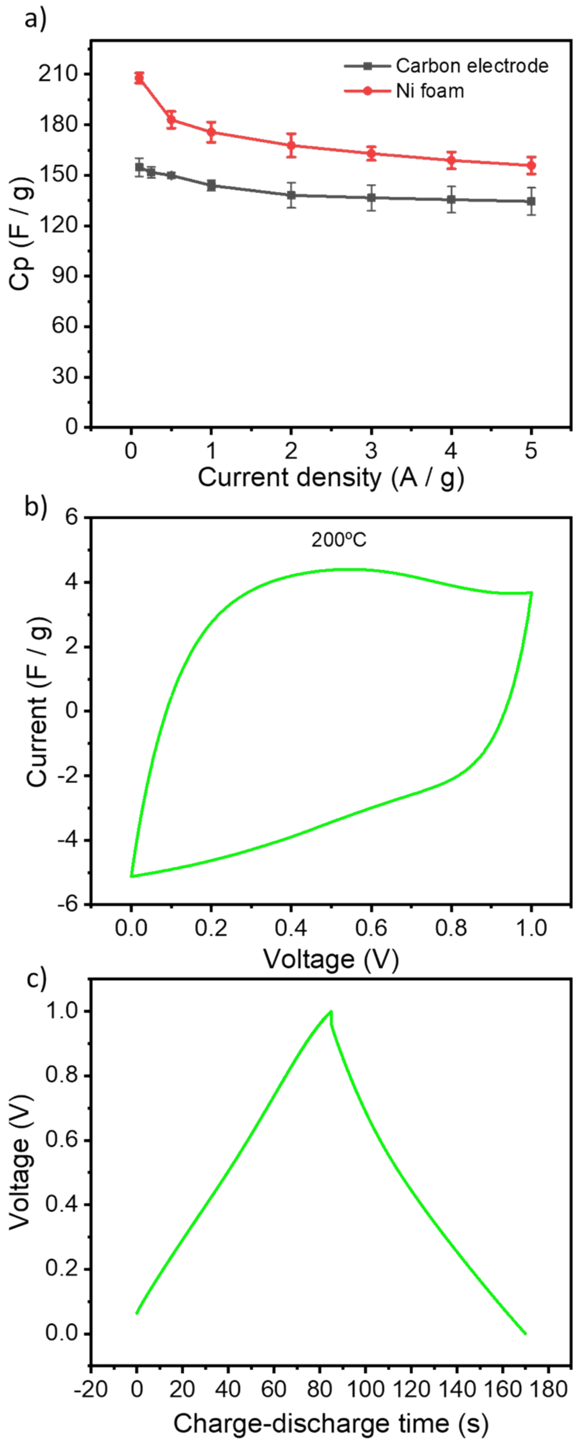

Figure S27. Current collector optimization for TrGO at 200ºC under air and KOH 6 M as electrolyte. (a) Comparison of specific capacitances versus current densities by using carbon electrode (black curve), and Ni foam (red curve). (b) CV curve at the scan rate of 50 mV/s and (c) GCD curves at the current density of 1 A/g by using Ni foam as current collector.

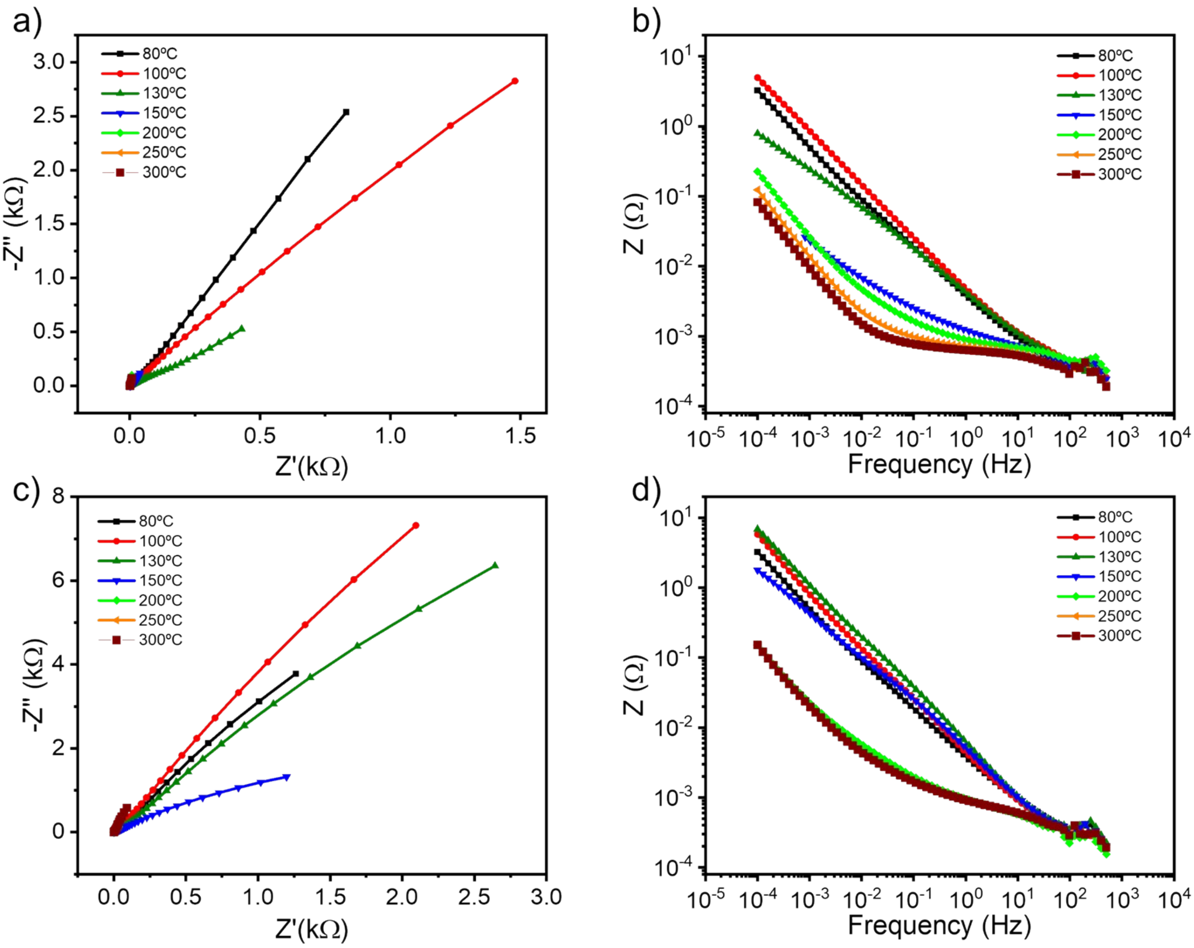

Figure S28. Nyquist and Bode plots of TrGO at different temperatures (a, c) under air and (b, d) under argon.

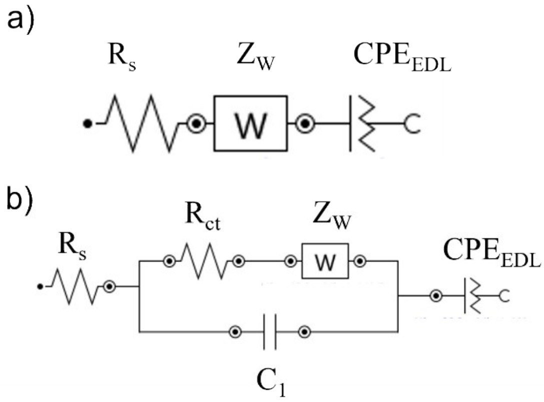

Scheme 1. The equivalent electric circuit models used for fitting the Nyquist plots. R_s: the intrinsic ohmic resistance; R_{ct}: charge transfer resistance; C_1: capacitance element; CPE_{EDL}: constant phase element representing the electrical double layer capacitance (EDLC); Z_w: a generalized finite Warburg element. The circuit a) is used to fit GO and TrGO under air (100-130ºC) and under argon (100-150ºC) samples. The circuit b) is used to fit TrGO under air (150-300ºC) and under argon (200-300ºC) samples.

Table S7. Fitting parameters obtained from the Nyquist plots.

Annealing temperature (ºC)	Air		Argon	
	Rs (mΩ)	Rct (mΩ)	Rs (mΩ)	Rct (mΩ)
80	207	-	207	-
100	308	-	198	-
130	193	-	247	-
150	288	364	202	-
200	300	387	195	366
250	238	346	201	380
300	238	346	208	406

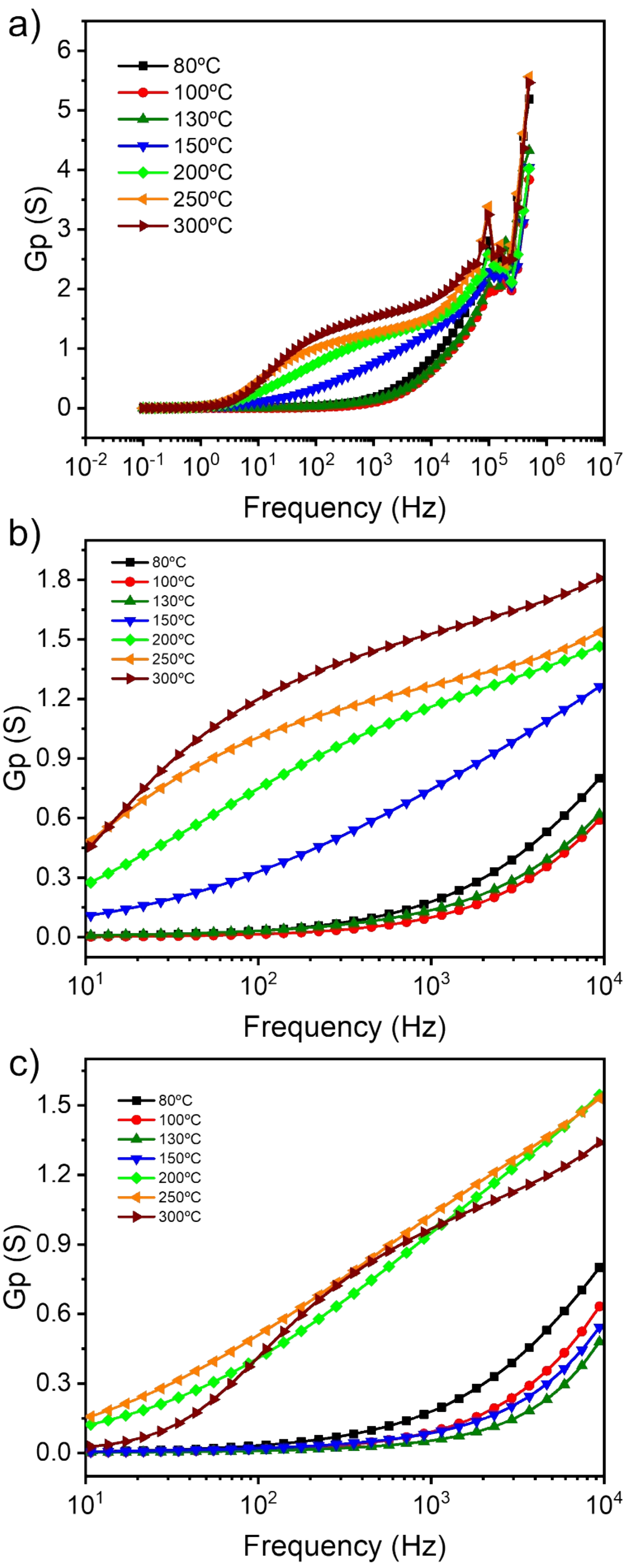

Figure S29. Conductance plots of TrGO at different temperatures (a, b) under air and (c) under argon.

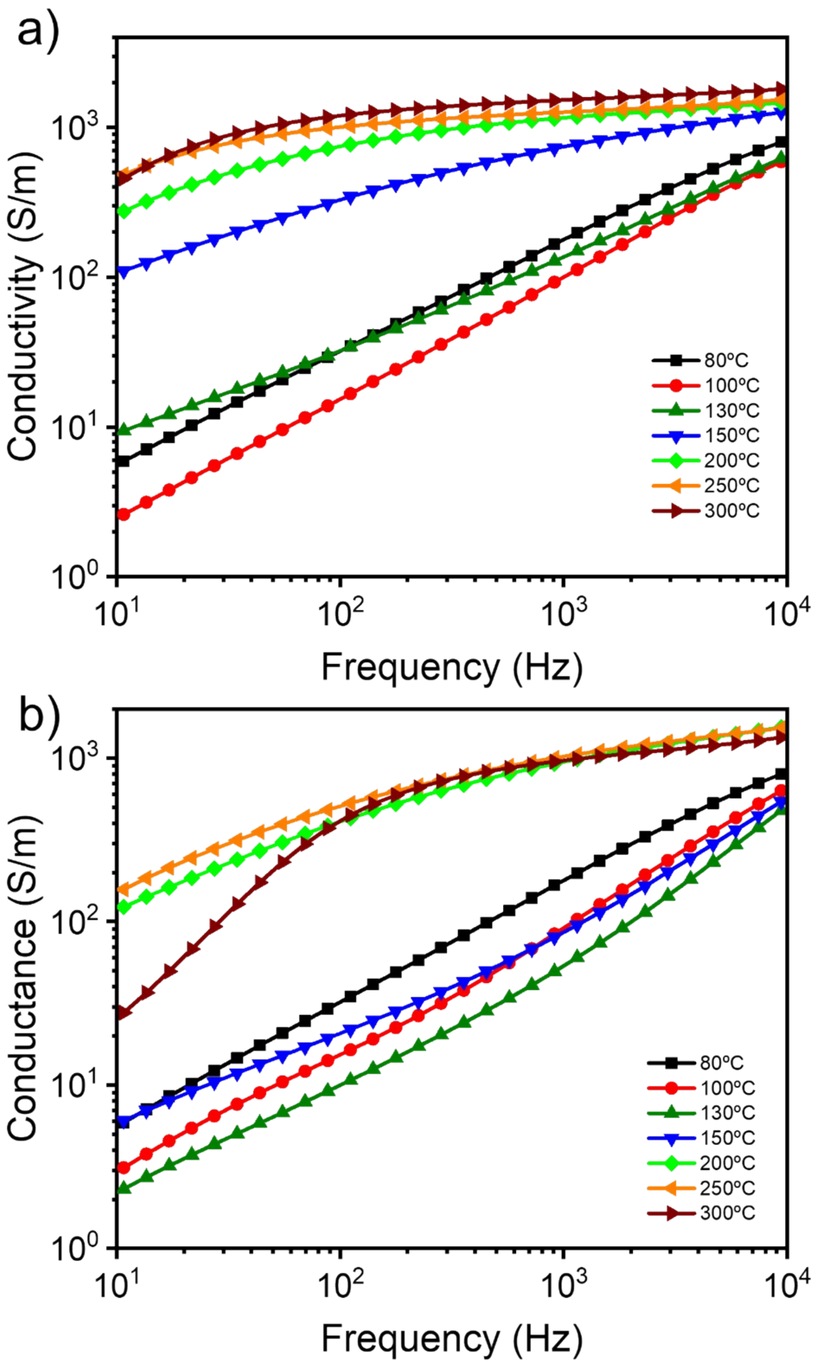

Figure S30. Conductivity plots of TrGO at different temperatures (a) under air and (b) under argon.

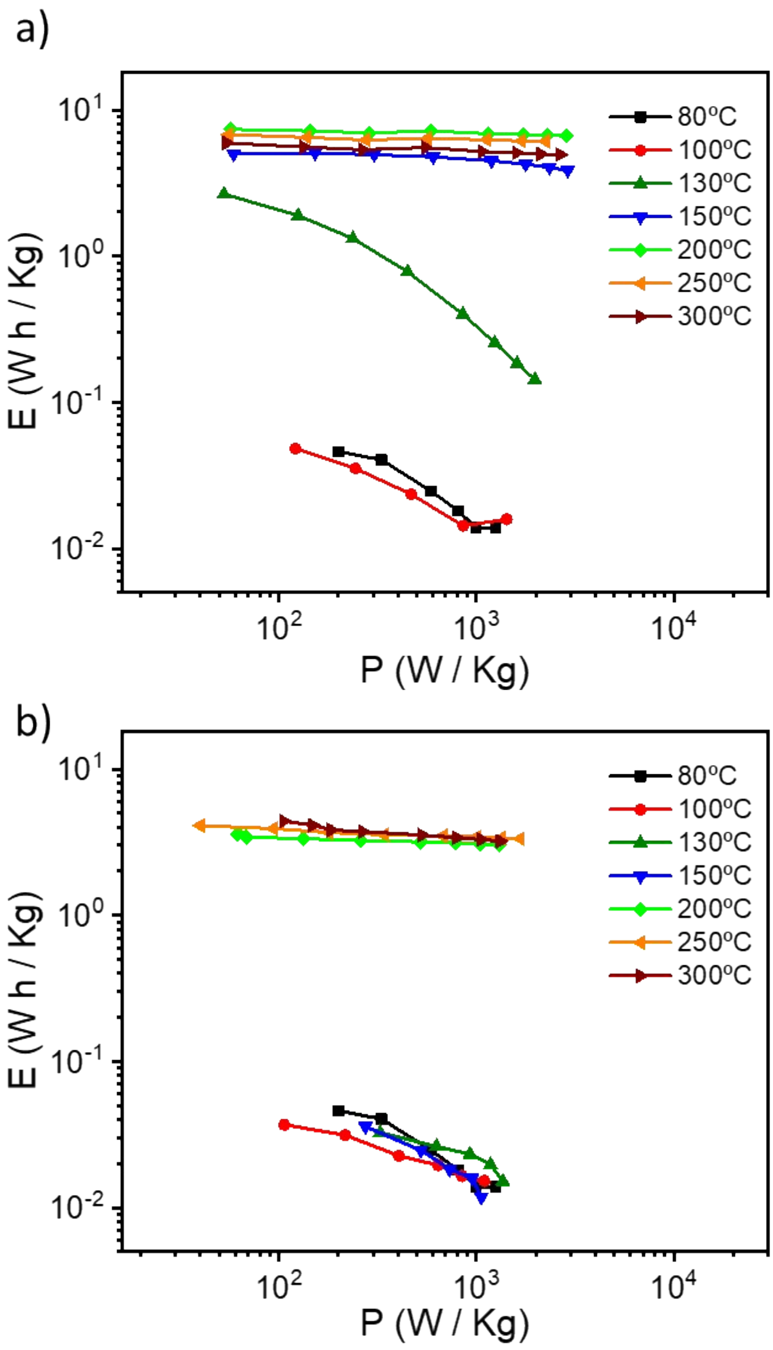

Figure S31. Ragone plot for TrGO at 200 °C (a) under air and (b) under argon.

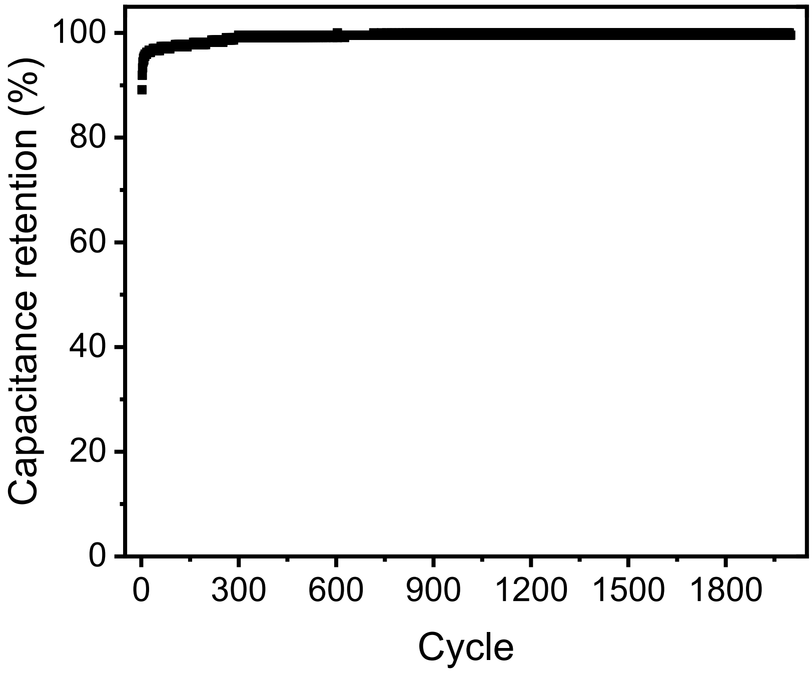

Figure S32. Cyclic stability of TrGO at 200ºC under air at the current density of 3 A/g.

References

1. I. Jung, D. A. Dikin, R. D. Piner and R. S. Ruoff, *Nano Lett.*, 2008, **8**, 4283-4287.
2. C. Mattevi, G. Eda, S. Agnoli, S. Miller, K. A. Mkhoyan, O. Celik, D. Mastrogiovanni, G. Granozzi, E. Garfunkel and M. Chhowalla, *Adv. Funct. Mater.*, 2009, **19**, 2577-2583.
3. I. Jung, D. A. Field, N. J. Clark, Y. Zhu, D. Yang, R. D. Piner, S. Stankovich, D. A. Dikin, H. Geisler, C. A. Ventrice and R. S. Ruoff, *J. Phys. Chem. C*, 2009, **113**, 18480-18486.
4. W. Chen and L. Yan, *Nanoscale*, 2010, **2**, 559-563.
5. K. Yin, H. Li, Y. Xia, H. Bi, J. Sun, Z. Liu and L. Sun, *Nano-Micro Lett.*, 2011, **3**, 51-55.
6. B. Zhao, P. Liu, Y. Jiang, D. Pan, H. Tao, J. Song, T. Fang and W. Xu, *J. Power Sources*, 2012, **198**, 423-427.
7. P. V. Kumar, N. M. Bardhan, S. Tongay, J. Wu, A. M. Belcher and J. C. Grossman, *Nature Chem.*, 2014, **6**, 151-158.
8. Y. Qiu, F. Guo, R. Hurt and I. Külaots, *Carbon*, 2014, **72**, 215-223.
9. B. C. Kim, W. J. Cho, W. G. Lee, S. J. Kim, R. Jalili, S. Y. Park, G. G. Wallace, K. H. Yu and S. J. Chang, *Synth. Met.*, 2014, **193**, 110-116.
10. A. M. Jastrzębska, J. Karcz, R. Letmanowski, D. Zabost, E. Ciecierska, J. Zdunek, E. Karwowska, M. Siekierski, A. Olszyna and A. Kunicki, *Appl. Surf. Sci.*, 2016, **362**, 577-594.
11. O. M. Slobodian, P. M. Lytvyn, A. S. Nikolenko, V. M. Naseka, O. Y. Khyzhun, A. V. Vasin, S. V. Sevostianov and A. N. Nazarov, *Nanoscale Res Lett* 2018, **13**, 139.
12. M. Tas, Y. Altin and A. Celik Bedeloglu, *Diam. Relat. Mater*, 2019, **92**, 242-247.
13. V. M. Maphiri, G. Rutavi, N. F. Sylla, S. A. Adewinbi, O. Fasakin and N. Manyala, *Nanomaterials*, 2021, **11**, 1909.
14. D. J. Lim, N. A. Marks and M. R. Rowles, *Carbon*, 2020, **162**, 475-480.
15. W. Lv, D. M. Tang, Y. B. He, C.-H. You, Z.-Q. Shi, X. C. Chen, C.-M. Chen, P. X. Hou, C. Liu and Q. H. Yang, *ACS Nano*, 2009, **3**, 3730-3736.
16. Z. Li, S. Gadipelli, Y. Yang and Z. Guo, *Small*, 2017, **13**, 1702474.
17. L. P. Bakos, L. Sárvári, K. László, J. Mizsei, Z. Kónya, G. Halasi, K. Hernádi, A. Szabó, D. Berkesi, I. Bakos and I. M. Szilágyi, *Nanomaterials*, 2020, **10**, 2313.
18. L. T. Le, M. H. Ervin, H. Qiu, B. E. Fuchs and W. Y. Lee, *Electrochem. commun.*, 2011, **13**, 355-358.
19. H. Zhang, V. V. Bhat, N. C. Gallego and C. I. Contescu, *ACS Appl. Mater. Interfaces*, 2012, **4**, 3239-3246.
20. H. Cao, X. Peng, M. Zhao, P. Liu, B. Xu and J. Guo, *RSC Adv.*, 2018, **8**, 2858-2865.